The Optic Nerve Head as a Biomechanical Structure: Initial Finite Element Modeling

Anthony J. Bellezza,[1] *Richard T. Hart,*[1] *and Claude F. Burgoyne*[1,2]

Purpose. To study the relationship between intraocular pressure (IOP) and the IOP-related stress (force/cross-sectional area) it generates within the load-bearing connective tissues of the optic nerve head.

Methods. Thirteen digital, three-dimensional geometries were created representing the posterior scleral shell of 13 idealized human eyes. Each three-dimensional geometry was then discretized into a finite element model consisting of 900 constituent finite elements. In five models, the scleral canal was circular (diameters of 0.50, 1.50, 1.75, 2.00, and 2.56 mm), with scleral wall thickness (0.8 mm) and inner radius (12.0 mm) held constant. In three models, the canal was elliptical (vertical-to-horizontal ratios of 2:1 [2.50 × 1.25 mm], 1.5:1 [2.1 × 1.4 mm], and 1.15:1 [1.92 × 1.67 mm]), with the same constant scleral wall thickness and inner radius. In five additional models, scleral canal size was held constant (1.92 × 1.67 mm), and either scleral wall thickness (three models, 0.5, 1.0, and 1.5 mm) or inner radius (two models, 13.0 and 14.0 mm) was varied. In all models, each finite element was assigned a single isotropic material property, either scleral (modulus of elasticity, 5500 kPa) or axonal (modulus of elasticity, 55 kPa). Maximum stresses within specific regions were calculated at an IOP of 15 mm Hg (2000 Pa).

Results. Larger scleral canal diameter, elongation of the canal, and thinning of the sclera increased IOP-related stress for a given level of IOP. For all models, maximum IOP-related stress ranged from 6 × IOP (posterior sclera) to 122 × IOP (laminar trabeculae). For each model, maximum IOP-related stress was highest within the laminar trabecular region and decreased progressively through the laminar insertion, peripapillary scleral, and posterior scleral regions. Varying the inner radius had little effect on the maximum IOP-related stress within the scleral canal.

Conclusions. Initial finite element models show that IOP-related stress within the load-bearing connective tissues of the optic nerve head is substantial even at low levels of IOP. Although the data suggest that scleral canal size and shape and scleral thickness are principal determinants of the magnitude of IOP-related stress within the optic nerve head, models that incorporate physiologic scleral canal and laminar geometries, a more refined finite element model meshwork, and nonisotropic material properties will be required to confirm these results. (*Invest Ophthalmol Vis Sci.* 2000;41:2991–3000)

The methodology for clinically determining the susceptibility of an optic nerve head (ONH) to a given level of 24-hour IOP does not exist. At present, not only is it impossible to assess 24-hour IOP exposure in a physiologic manner, but there is also no agreement on the relationship between the measured IOP and the propensity of an eye to develop vision-threatening damage.

We have begun to model the optic nerve head as a biomechanical structure. Our approach evolves from the hypothesis that even at normal levels of IOP, the connective tissues of the ONH are constantly exposed to substantial levels of IOP-related stress (force/cross-sectional area). The level of stress generated by normal levels of IOP is assumed to play a central role in the physiology and, in some eyes, the pathophysiology of all three ONH tissue types: connective (load-bearing connective tissues of the peripapillary sclera, scleral canal wall, and lamina cribrosa), axonal (retinal ganglion cell axons), and cellular (astrocytes, glial cells, endothelial cells, and pericytes along with their basement membranes).

This biomechanical model suggests that a given level of IOP-related stress may be physiologic or pathophysiologic depending on the individual ONH experiencing the stress. Physiologic levels of IOP-related stress are assumed to be capable of inducing a broad spectrum of acute and chronic changes in all three ONH tissue types that are central to normal ONH aging. Pathophysiologic levels of IOP-related stress are assumed to

---

From the [1]Department of Biomedical Engineering, Tulane University, New Orleans, Louisiana; and the [2]Louisiana State University Eye Center, Louisiana State University Health Sciences Center, New Orleans.

Presented in part at the annual meeting of the Association for Research in Vision and Ophthalmology, Fort Lauderdale, Florida, May 1998.

Supported in part by US Public Health Service Grants R01EY11610 and P30EY02377 from the National Eye Institute, National Institutes of Health, (CFB); a grant from the American Health Assistance Foundation, Rockville, Maryland (CFB); a grant from The Whitaker Foundation, Rosslyn, Virginia (CFB); a Career Development Award (CFB) and an unrestricted departmental grant (LSU Eye Center) from Research to Prevent Blindness, New York, New York; and a graduate student stipend from the Board of Regents, State of Louisiana (AJB).

Submitted for publication August 31, 1999; revised March 6, 2000; accepted March 31, 2000.

Commercial relationships policy: N.

Corresponding author: Claude F. Burgoyne, LSU Eye Center, 2020 Gravier Street, Suite B, New Orleans, LA 70112. cburgo@lsuhsc.edu

induce pathologic changes in cell synthesis and tissue microarchitecture that underlie the two governing pathophysiologies in glaucomatous damage: mechanical failure of the load-bearing connective tissues of the ONH, and progressive damage to the adjacent axons (with eventual retinal ganglion cell death) by a combination of both compressive and ischemic mechanisms.

From a basic biomechanical standpoint, stress generates strain (tissue deformation in response to load) within tissues that experience load. The magnitude of strain is based on the material properties of the tissues, including how well the tissues are able to resist deformations induced by the applied stress. Tissues are physically damaged (undergo mechanical failure) in a predictable manner and pattern as the level of strain exceeds the tissues' elastic limits.

We hypothesize that, within the ONH, the connective tissues of the peripapillary sclera, scleral canal wall, and lamina cribrosa are damaged in a predictable pattern by IOP-related stress and strain. The model suggests that it is the predictable pattern of mechanical failure within the connective tissues that underlies the clinical appearance of a glaucomatous ONH (progressive posterior bowing and excavation of the ONH tissues beneath the anterior scleral canal opening). We further hypothesize that axons are damaged by both the direct and indirect effects of IOP-related stress through a variety of mechanisms. These mechanisms include not only the classic notion of physical compression (either external compression by intact laminar beams[1,2] or spontaneous compression, in which differences in tissue pressure across the lamina cause axons to collapse spontaneously[3]) but also both acute and chronic ischemia,[4,5] which may be induced by the effects of IOP-related stress and strain on blood flow and diffusion within the connective tissues through which the ONH blood supply must pass.[6]

The model thus suggests that estimating the maximum level of IOP-related stress for a given patient's ONH (for a given level of IOP) will become an important step in the clinical estimation of the susceptibility of an individual ONH to glaucomatous damage at that level of IOP. As a first step toward building the clinical methodology to make this estimation, we have begun to use analytical and computational models (finite element models [FEMs]) to study the relationship between IOP and IOP-related stress within the load-bearing connective tissues of the ONH.

Analytical models based on linear elasticity theory are useful for idealized investigations of the eye as a mechanical structure. However, because idealized models cannot accurately account for the complex geometry, material property distributions, and mechanical loading in the eye, approximate computational methods are needed.

The finite element method is a computer-based engineering method that has been used to study the mechanical behavior of structures with complex geometries and material properties[7] (Fig. 1). An FEM includes the important aspects of three-dimensional (3D) geometry, material properties, boundary conditions, and mechanical loads. These models are based on a digital 3D geometry that approximates the structure being modeled, which is discretized into small, regularly shaped, "building blocks" (the finite elements) whose boundaries connect points within the geometry (called nodes). Each finite element of the model is assigned its own shape and material properties (the characteristics of its connective tissue composition that determine the element's behavior under load). The mechanical behavior of the total structure is then calculated from the combined behavior of its constituent finite elements.

The principal goal of building an FEM is to determine the mechanical response (e.g., deformation, constitutive stresses and strains) of a complex structure subjected to a variety of loading conditions. Although the finite element method is an approximate method, the degree of the approximation can be controlled, and this approach often represents the only practical solution method for complex structures.[7]

The modeling of a complex biologic structure is best performed by starting with simple models that capture the most important aspects of its structure. The model is then refined by adding features such as nonlinear material properties, more physiologically accurate geometries, and secondary loading conditions, to more accurately capture the structure's responses to load.

In this report we present data for the maximum levels of IOP-related stress within four regions of the posterior scleral shell for 13 different FEMs, which, taken together, span the published range of variation in the 3D anatomy of the human scleral canal and posterior scleral shell.[8–10]

MATERIALS AND METHODS

Idealized Analytical Model

As a first step, simple analyses of the eye as an idealized spherical shell were considered. Within the wall of any pressurized spherical shell, the two principal stresses reside within the plane of the vessel wall (the third stress is radial in direction and minimal in magnitude; Fig. 2). For a thin-walled vessel (defined as having a wall thickness ≤ 0.1 of the radius), linear elasticity theory predicts that the planar wall stresses are equal and orthogonal and that each stress can be approximated by the equation

$$\sigma = \frac{PR}{2t} \qquad (1)$$

where P is the inner pressure (IOP), R is the inner radius of the sphere (approximately one half the axial length), and t is the thickness of the vessel wall (scleral thickness).[11]

Estimating IOP-related stress within and around the load-bearing connective tissues of the scleral canal using analytical models is more complex. A simple closed-form solution of the thin-walled spherical shell stress equation is no longer feasible, because the geometry of the ONH and its load-bearing tissues is too complex. However, a close analogy to this geometry for which we can compute an analytical solution is the case of an elliptical hole within a flat plate that is under tension at two ends. In this idealized case, it can be shown that the maximum stress always occurs at the edge of the hole along the long axis of the ellipse, and has a value of

$$\sigma = S\left(1 + \frac{2a}{b}\right) \qquad (2)$$

where S is the stress applied to the ends of the plate, a is the length of the long axis, and b is the length of the short axis.[11]

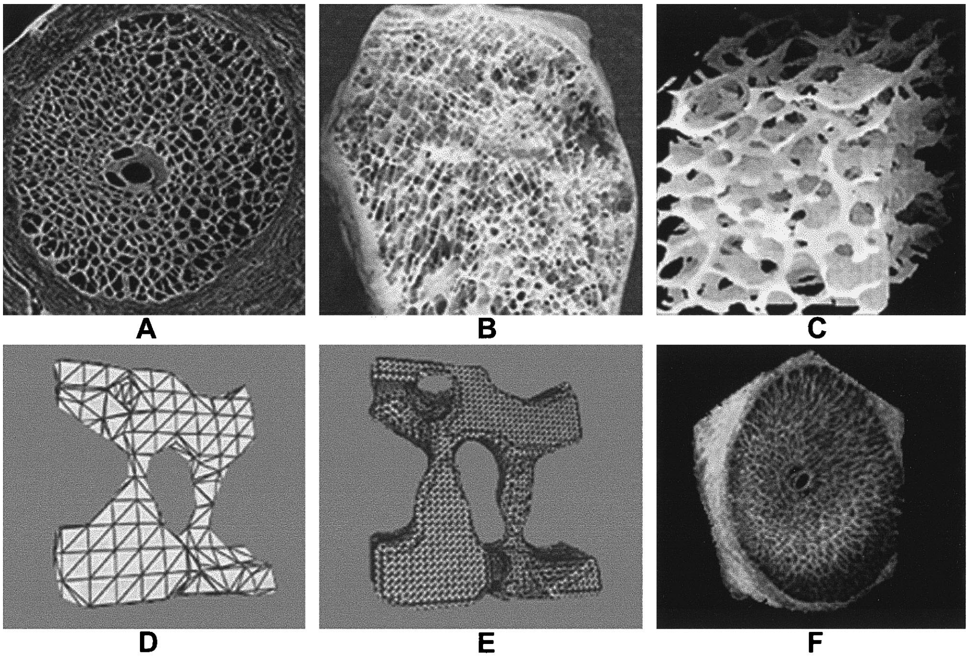

Figure 1. The 3D microarchitecture of the lamina cribrosa **(A)** is similar to that of trabecular bone **(B),** which has been modeled using finite element methodology and serves as an example of the process. **(C)** Finite element modeling starts with a digital 3D geometry that approximates the microarchitecture of the object being modeled, seen here in this digital reconstruction of serial histologic sections of trabecular bone. **(D)** The 3D geometry of the model is then subdivided into a series of individual finite elements, seen in a close-up of two individual trabeculae subdivided into their constituent finite elements. **(E)** Progressive refinement of the model with larger numbers of elements increases its accuracy. Although the geometries of the posterior scleral shell were constructed using idealized human dimensions (see Fig. 3), the next generation of models will incorporate geometries based on 3D reconstructions of serial histologic sections of the load-bearing tissues of the ONH, as seen in **(F)**, which is a digital, 3D reconstruction of 64 serial, 5-μm histologic sections of a monkey ONH, in which the connective tissues of each section have been stained and then isolated by thresholding. **(A)**, Reprinted with permission from Minckler DS. Histology of optic nerve damage in ocular hypertension and early glaucoma (summary). *Surv Ophthalmol.* 1989;33: 401–402. **(C)**, Reprinted with permission from Odgaard A, et al. A direct method for fast three-dimensional serial reconstruction. *J Microsc.* 1990;159;335–342. © The Royal Microscopical Society. **(D, E)**, Reprinted with permission from Müller R, et al. Noninvasive bone biopsy: a new method to analyze and display the three-dimensional structure of trabecular bone. *Phys Med Biol.* 1994;39:145–164. © IOP Publishing, Ltd.

FEM Geometry

For these initial analyses, 13 models (Table 1 and Fig. 3) representing the posterior shell of 13 idealized human eyes were developed by computer with finite element preprocessing software (Truegrid; XYZ Scientific Applications, Livermore, CA). For eight of the FEMs (M1–M8, Table 1), a standard posterior scleral shell with an inner radius of 12.0 mm and wall thickness of 0.8 mm was constructed (Figs. 3A, 3B) and the size and shape of the scleral canal opening were varied (Fig. 4), using dimensions that span the range of values reported for the human scleral canal.[8–10] In three additional models (M9, M10, and M11) the scleral canal geometry (1.92 × 1.67 mm) and inner radius (12.0 mm) of model M8 were used, with variable scleral wall thickness (M9, 0.5 mm; M10, 1.0 mm; M11, 1.5 mm). For the final two models (M12, M13), the scleral canal geometry (1.92 × 1.67 mm) and scleral thickness (0.8 mm) of model M8 were used, and the inner radius of the posterior scleral shell was varied (M12, 13.0; M13, 14.0 mm).

For these 13 initial models, the scleral shell consisted of two layers of finite elements (inner and outer layer elements,

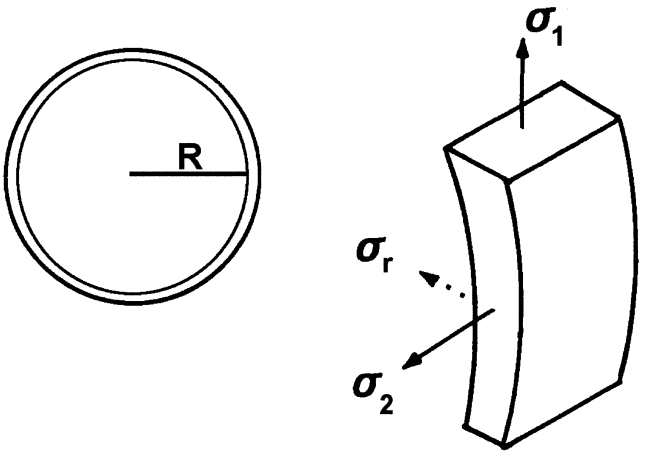

Figure 2. Depiction of principal stresses within a thin-walled spherical pressure vessel of radius R. The two largest principal stresses, σ_1 and σ_2, are equal, at right angles to each other, and reside within the plane of the wall. The third principal stress, σ_r, is minimal in magnitude and directed toward the center of the sphere.

Table 1. Dimensions for Each of the 13 FEMs

	Scleral Canal			Scleral Shell	
Model	Shape	Dimensions (mm)	Cross-Sectional Area (mm^2)	Inner Radius (mm)	Wall Thickness (mm)
M1	Circular	0.50 × 0.50	0.20	12.0	0.8
M2	Circular	1.50 × 1.50	1.77	12.0	0.8
M3	Circular	1.75 × 1.75	2.41	12.0	0.8
M4	Circular	2.00 × 2.00	3.14	12.0	0.8
M5	Circular	2.56 × 2.56	5.15	12.0	0.8
M6	Elliptical	2.50 × 1.25	2.45	12.0	0.8
M7	Elliptical	2.10 × 1.40	2.31	12.0	0.8
M8	Elliptical	1.92 × 1.67	2.52	12.0	0.8
M9	Elliptical	1.92 × 1.67	2.52	12.0	0.5
M10	Elliptical	1.92 × 1.67	2.52	12.0	1.0
M11	Elliptical	1.92 × 1.67	2.52	12.0	1.5
M12	Elliptical	1.92 × 1.67	2.52	13.0	0.8
M13	Elliptical	1.92 × 1.67	2.52	14.0	0.8

Fig. 3), whereas tissues within the scleral canal were a single element thick and were positioned confluent with the outer layer of the scleral shell. The lamina cribrosa was represented by a grid of broad connective tissue strips one element thick spanning the posterior aspect of the scleral canal (Fig. 3C).

Finite Element Refinement

Because the finite element solutions are numerical approximations, questions about the nature of the approximation must be addressed. The derivation of the displacement-based finite element method shows that for a given 3D geometry, increasing the number of constituent finite elements increases the accuracy of the solution (Figs. 1D, 1E).[7] Thus, to determine the appropriate number of elements needed for accurate solutions, a convergence test can be performed as follows: The geometry of the structure is modeled using a series of increasingly refined finite element meshes. During the analysis of each model, the displacements at identical locations of the structure are calculated for the different meshes. The calculated solutions using the more refined meshes are more accurate, but there is also a point of diminishing returns when increasing refinement provides little improvement in the calculated solutions. When this level of accuracy is reached, the model is judged sufficiently refined. Using this methodology, element meshes made up of 900 elements provided acceptable displacement values (data not shown). As such, each of the 13 models in this report consists of 900 elements, although the 3D geometry of each element is not identical from one model to another, because of the overall variation in model geometry.

Material Property Assignment

In these initial models, the constituent finite elements were subdivided into two tissue types: axonal (non–load-bearing scleral canal elements within the fenestrations of the connective tissue grid, Fig. 3C) and connective (load-bearing elements within the sclera, scleral canal wall, and the scleral canal connective tissue grid, Fig. 3C). A single material property was then assigned to each element based on its tissue type. The scleral material property (modulus of elasticity of 5500 kPa) was based on scleral mechanical testing data previously reported by Kobayashi et al.[12] The axonal material property (modulus of elasticity of 55 kPa) was chosen to be two orders of magnitude less to reflect the fact that the axons are likely to be compliant and unlikely to bear significant load.

FEM Boundary and Operating Conditions

To prevent rigid body motion of the model, the nodes along the base of the model (representing the transverse or anterior–posterior equator of the eye) were constrained to radial movement only, whereas all other nodes were allowed to move freely in any direction. All simulations were run at an IOP of 2.0 kPa (15 mm Hg) on a computer workstation (Origin; Silicon Graphics, Mountain View, CA) using finite element analysis software (Abaqus ver. 5.8; Hibbit, Karlsson, and Sorensen, Pawtucket, RI). Postprocessing analysis was performed using Abaqus/Post (Hibbit, Karlsson, and Sorensen).

IOP-Related Stress Calculations by Integration Point and Region

Within each finite element of each model, the FEM software characterized stress at 27 distinct integration points (Figs. 3D, 3E). We defined the stress magnitude at each integration point to be the magnitude of the vector sum of the three principal stresses acting at that point. For each model, therefore, stress magnitude was determined at a total of 24,300 points (900 elements × 27 integration points/element).

To characterize the maximum stress by region within each model, the finite elements of each model were subcategorized into four regions (Fig. 5). The laminar trabecular region (Fig. 5A) was defined to include all the connective tissue finite elements within the scleral canal. The laminar insertion region (Fig. 5B) was defined to include the single most peripheral element of each laminar beam as well as the single row of elements of the scleral shell immediately adjacent to the scleral canal. The peripapillary scleral region (Fig. 5C) was defined to include all finite elements in the second, third, and fourth rows outside the scleral canal (extending from approximately 1 mm to 3 mm away from the scleral canal). Finally, the posterior scleral region (not shown) was defined to include all the remaining finite elements of the posterior scleral shell (extending from the fifth row of elements away from the canal to the elements of the transverse equator).

The stress magnitudes from all the integration points within each region were analyzed and a top 5% value for

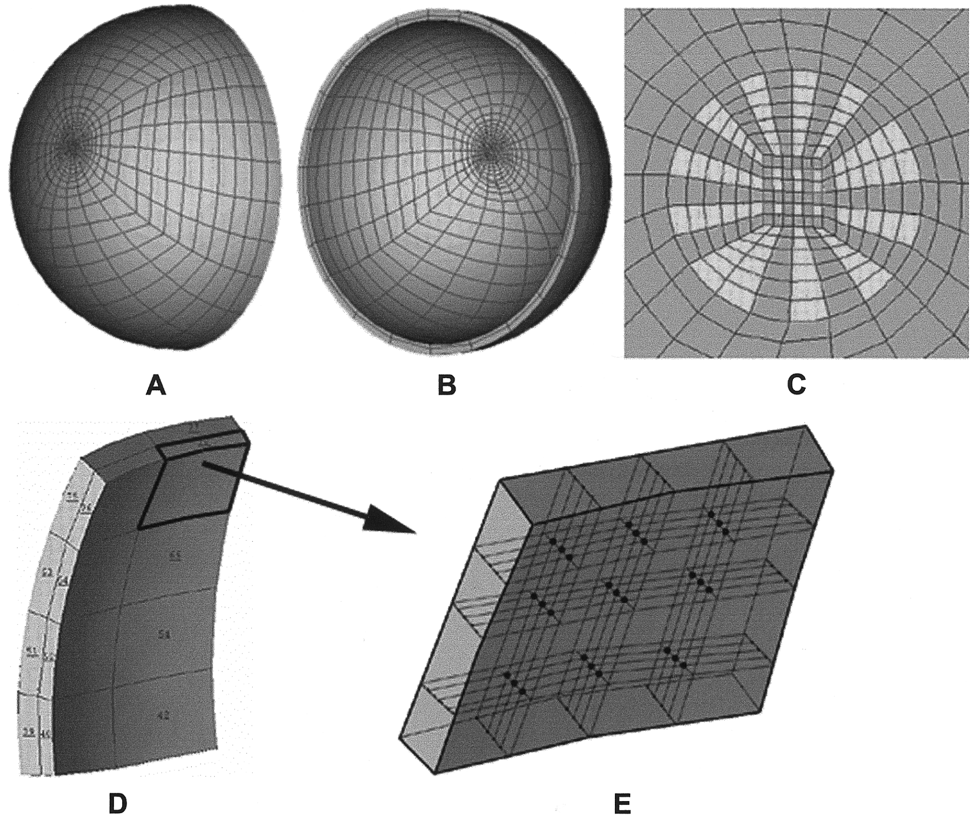

FIGURE 3. Views of the external (**A**) and internal (**B**) surfaces of our standard posterior scleral shell geometry. The thickness of the shell is made up of two finite elements: an inner element and an outer element. (**C**) A close-up of the scleral canal of one model (M3, Fig. 4) shows the finite element arrangement within and around the ONH. Although it is not clearly shown by this figure, within the scleral canal there is only a single, posterior (outer) layer of elements depicting the relatively posterior position of the lamina cribrosa as it is situated within the human scleral canal. Darker shaded elements are those assigned scleral material properties, whereas lighter shaded elements model the axonal bundles within the laminar fenestrations and are assigned axonal material properties. (**D, E**) A close-up of one element from the posterior scleral wall displays the 27 internal integration points that are found within each finite element of the model. Note the three layers of integration points within each element (**E**). The stress magnitude is calculated at each of these integration points and is defined as the vector sum of the three principal stresses acting at that point. Maximum IOP-related stress within a region (Fig. 5) is assessed by pooling the stress magnitude values from all the integration points from all the finite elements within that region and reporting the mean of the top 5% of the stress magnitude values assessed.

maximum stress within a region was defined to be the mean of the highest 5% of stress magnitude values within the region and was intended to conservatively estimate the highest level of stress. Maximum stresses for the laminar insertion and the peripapillary scleral regions were also subcategorized in terms of superior–inferior and nasal–temporal regions (Fig. 5C).

RESULTS

When the standard, human posterior scleral shell geometry with an inner radius of 12.0 mm and a scleral wall thickness of 0.8 mm is used, equation 1 yields principal planar wall stresses (σ_1 and σ_2, Fig. 2) of approximately 7.5 × IOP.

$$\sigma_1 = \sigma_2 = \frac{PR}{2t} = \frac{\mathrm{IOP}(12)}{2(0.8)} = 7.5 \times \mathrm{IOP} \qquad (3)$$

Combining these two principal stresses gives a total scleral shell wall stress magnitude of 10.6 × IOP, regardless of the level of IOP.

$$\sigma_{\mathrm{sclera}} = \sqrt{(\sigma_1)^2 + (\sigma_2)^2} = 10.6 \times \mathrm{IOP} \qquad (4)$$

These analytical equations show that increases in the inner radius and decreases in scleral wall thickness further elevate IOP-related stress within the scleral wall at a given level of IOP.

The stresses (reported in kilopascals) for the posterior scleral shell, peripapillary sclera, laminar insertion zone, and laminar trabeculae (Table 2) are the FEM estimates of the maximum stress magnitudes present within these tissues when the IOP is 15 mm Hg (2.0 kPa). Table 3 summarizes the relationship of maximum IOP-related stress to IOP for each region.

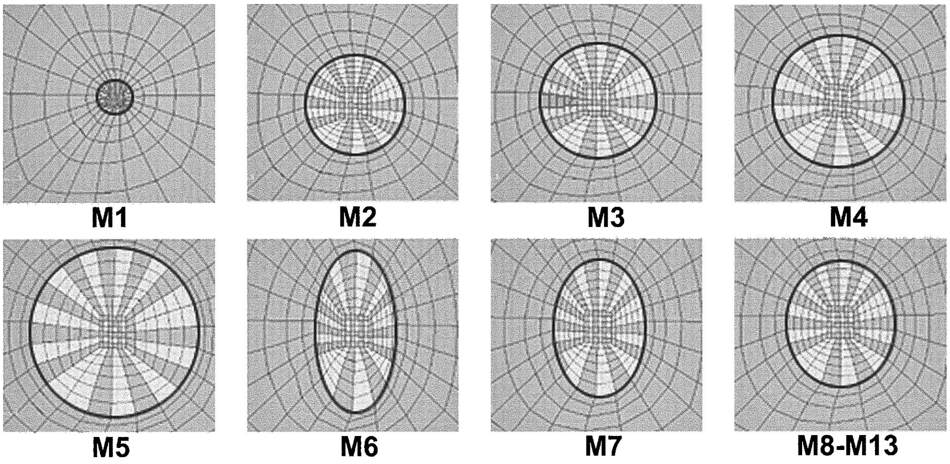

FIGURE 4. Dimensions of scleral canal geometries (depicted to scale). A heavy line outlines the scleral canal for all models. Darker shaded elements are those with scleral material properties, whereas lighter shaded elements have axonal material properties. The peripapillary and posterior scleral shell (outside of the scleral canal) are two finite elements thick. Although it is not clearly depicted in this figure, within the scleral canal there is only a single, posterior (outer) layer of elements depicting the relatively posterior position of the lamina cribrosa as it is situated within the human scleral canal. Note that because of the relative crudeness of the laminar geometry, horizontally aligned laminar beams are consistently thinner than the vertically aligned beams within models containing elliptical scleral canals (models M6, M7, and M8–M13).

Posterior Scleral Wall Stress

The maximum stress within the posterior scleral shell (away from the peripapillary sclera) for models M1 through M5 (circular scleral canals) and models M6, M7, and M8 (elliptical scleral canals) was approximately 11 times the level of IOP for each model (Tables 2 and 3).

In models M8 through M11, the radius (12.0 mm) and scleral canal geometry (1.92 mm × 1.67 mm) were held constant, and scleral wall thickness was varied between 0.5 and 1.5 mm. The data suggest that posterior scleral wall stress increased in eyes with thin sclera and decreased in eyes with thick sclera. When scleral wall thickness was held constant at 0.8 mm (models M8, M12, and M13), posterior scleral wall stress increased slightly as the size of the posterior scleral shell increased (from 11 × IOP for an inner radius of 12.0 mm to 13 × IOP for an inner radius of 14.0 mm).

Peripapillary Scleral Wall Stress

Unlike the posterior sclera away from the canal, IOP-related stress within the peripapillary sclera was profoundly influenced by the size and shape of the scleral canal (Table 2). Increasing the size of a circular canal increased peripapillary

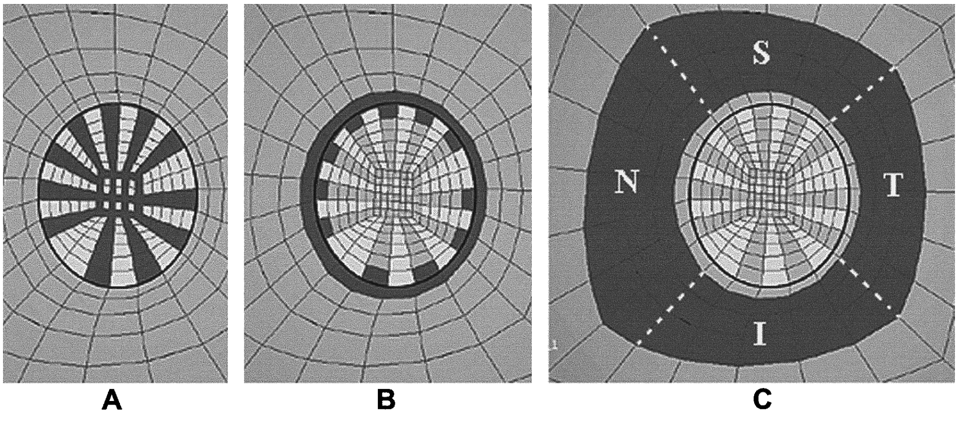

FIGURE 5. Our strategy for grouping elements into regions. (**A**) The laminar trabecular region encompasses the darkly colored elements, which make up the laminar beams. (**B**) The laminar insertion region includes the most peripheral element from each laminar beam, as well as all the finite elements immediately adjacent to the scleral canal wall (one finite element into the peripapillary sclera). (**C**) The peripapillary scleral region is defined as the region from the second to the fourth elements outside the canal wall. The posterior scleral region (not shown) consists of a subset of elements evenly spaced throughout the scleral wall. The laminar insertion region and the peripapillary scleral region were further subdivided into superior–inferior (S, I) and nasal–temporal (N, T) areas.

TABLE 2. Maximum Stress Values

Model	Posterior Scleral Wall Stress	Maximum PPS Stress	Maximum Laminar Insertion Stress	Maximum Laminar Trabecular Stress
Circular				
M1 (0.50 × 0.50)	21.5	22.6	40.5	68.1
M2 (1.50 × 1.50)	21.5	29.7	61.0	107.2
M3 (1.75 × 1.75)	21.5	31.7	68.7	129.5
M4 (2.00 × 2.00)	21.5	33.8	76.7	154.1
M5 (2.56 × 2.56)	21.4	39.5	94.6	215.0
Elliptical				
M6 (2.50 × 1.25)	21.5	41.1	79.4	144.4
M7 (2.10 × 1.40)	21.5	34.1	70.6	130.1
M8 (1.92 × 1.67)	21.5	32.3	70.4	133.7
Wall thickness				
M9 (0.5)	34.4	53.2	126.5	243.8
M8 (0.8)	21.5	32.3	70.4	133.7
M10 (1.0)	17.2	25.4	53.1	99.2
M11 (1.5)	11.7	16.3	31.8	56.7
Inner radius				
M8 (12.0)	21.5	32.3	70.4	133.7
M12 (13.0)	23.2	33.9	73.0	132.8
M13 (14.0)	25.0	35.6	75.7	132.8

All dimensions given in millimeters. Data are in kilopascals (15 mm Hg = 2.0 kPa) and are the mean of the highest 5% of stress magnitude values within each region. PPS, peripapillary sclera.

scleral stress from approximately 11 × IOP (0.50 × 0.50 mm canal, model M1) to 20 × IOP (2.56 × 2.56 mm canal, model M5; Table 3).

For two canals with similar cross-sectional areas (models M3 and M6, Table 1), peripapillary scleral stress was higher for the more elliptical canal (M6, 21 × IOP; M3, 16 × IOP; Table 3). Furthermore, within the peripapillary scleral region, maximum stresses near the vertical axis of all elliptical scleral canals were consistently greater than those found nasally and temporally. In the most elongated ellipse (model M6, canal dimension 2.50 × 1.25 mm), the maximum superior–inferior peripapillary scleral stresses were 49% higher than the nasal–temporal values (data not shown).

For the mean human canal dimensions (model M8), decreasing wall thickness from 1.5 mm to 0.5 mm increased peripapillary scleral stress from 8 to 27 × IOP (models M11–M8, Table 3). However, increasing the size of the posterior shell from an inner radius of 12.0 to 14.0 mm (models M8, M12, and M13) only minimally increased peripapillary scleral stress.

Laminar Insertion Stress

Laminar insertion stress was profoundly influenced by the size of the scleral canal (Tables 2 and 3). Increasing the size of a circular canal increased maximum laminar insertion zone stress from approximately 20 × IOP (model M1, 0.50 × 0.50 mm canal) to 47 × IOP (model M5, 2.56 × 2.56 canal; Table 3).

TABLE 3. Summary of the Maximum Stress Levels Expressed as Multiples of IOP

Model	Posterior Sclera	Peripapillary Sclera	Laminar Insertion Zone	Laminar Trabeculae
Circular				
M1 (0.50 × 0.50)	11	11	20	34
M2 (1.50 × 1.50)	11	15	31	54
M3 (1.75 × 1.75)	11	16	34	65
M4 (2.00 × 2.00)	11	17	38	77
M5 (2.56 × 2.56)	11	20	47	107
Elliptical				
M6 (2.50 × 1.25)	11	21	40	72
M7 (2.10 × 1.40)	11	17	35	65
M8 (1.92 × 1.67)	11	16	35	67
Wall thickness				
M9 (0.5)	17	27	63	122
M8 (0.8)	11	16	35	67
M10 (1.0)	9	13	27	50
M11 (1.5)	6	8	16	28
Inner radius				
M8 (12.0)	11	16	35	67
M12 (13.0)	12	17	36	66
M13 (14.0)	13	18	38	66

All dimensions shown in millimeters. Data are the means of the highest 5% of stress magnitude values (from Table 2) expressed as multiples of IOP.

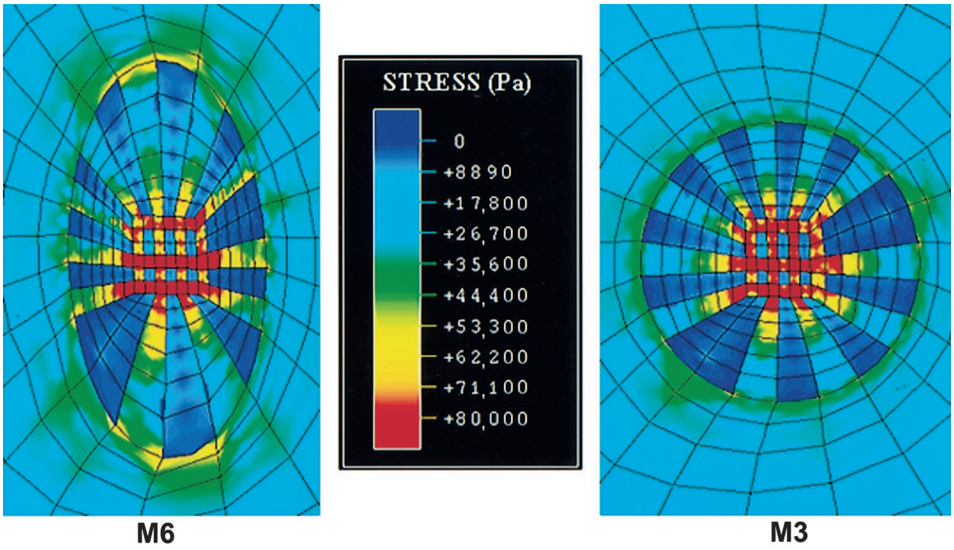

FIGURE 6. Contour plots showing stress magnitudes on the outer surface of two models with similar scleral canal cross-sectional areas, one with an elliptical scleral canal (left, M6, diameters of 2.50 × 1.25 mm) and one with a circular scleral canal (right, M3, diameters of 1.75 × 1.75 mm). Note that within the peripapillary scleral and laminar insertion regions of the two models, the highest stress magnitudes occur within the vertical and horizontal axes of the elliptical canal (model M6). Within model M6, the stresses at the horizontal axes are slightly higher than those at the vertical axis; however, this is most likely because at the edge of the canal, the finite elements along the horizontal axis are slightly smaller than those along the vertical axis. Unlike the peripapillary scleral and laminar insertion zone stresses, the laminar trabecular stresses are similar in magnitude in the elliptical and spherical models. Within both models, the highest laminar stress magnitudes occur within the finite elements of the small, central laminar beams. However, because the geometry of these models does not adequately reflect the complexity of the lamina cribrosa, the location and magnitude of the models' predictions for laminar stress may not be accurate.

Scleral canal shape also influenced the level of laminar insertion zone stress. For two canals with similar cross-sectional areas (models M3 and M6, Table 1), the maximum stress within the laminar insertion zone was 40 × IOP for the elliptical canal (model M6, Table 3) compared with 34 × IOP for the circular canal (model M3, Table 3).

In an eye with mean human scleral canal dimensions (model M8, 1.92 × 1.67 mm), decreasing wall thickness from 1.5 mm to 0.5 mm (models M8–M11) increased laminar insertion stress from 16 to 63 × IOP (Table 3). However, increasing the size of the posterior shell of the same model from an inner radius of 12.0 to 14.0 mm (models M8, M12, and M13) only minimally increased laminar insertion zone stress.

Laminar Stress

Stress within the laminar trabeculae was profoundly influenced by the size of the scleral canal. Maximum laminar stress increased from approximately 34 × IOP in a small circular canal (model M1, 0.50 × 0.50 mm canal) to 107 × IOP in a large one (model M5, 2.56 × 2.56 mm canal; Table 3).

However, unlike peripapillary scleral and laminar insertion zone stress, the maximum level of laminar stress was little influenced by the shape of the scleral canal (Fig. 6). For two canals with similar cross-sectional areas (models M3 and M6, Table 1), the maximum stress within the laminar trabecular region was 72 × IOP for the elliptical canal (model M6, Table 3) and 65 × IOP for the circular canal (model M3, Table 3).

For models with mean human scleral canal dimensions (1.92 × 1.67 mm), decreasing scleral wall (and laminar) thickness from 1.5 mm to 0.5 mm (models M11, M12, and M13) increased maximum laminar stress from 28 to 122 × IOP (Table 3). However, increasing the size of the posterior shell from an inner radius of 12.0 to 14.0 mm (models M8, M12, M13; Table 3) only minimally increased laminar stress.

DISCUSSION

In the present studies, we used an engineering technique called finite element modeling to estimate the stresses within 13 idealized human posterior scleral shell geometries at an IOP of 15 mm Hg (2.0 kPa). Our estimates of maximum IOP-related stress achieved levels of 27 to 122 × IOP within the tissues of the peripapillary scleral, laminar insertion, and laminar trabecular regions of these models. The results provide evidence in support of our hypothesis that the load-bearing tissues of the ONH are subject to substantial levels of IOP-related stress even at low levels of IOP.

To our knowledge, Greene[13] was the first to suggest that stresses within the peripapillary sclera might be concentrated relative to the more peripheral posterior sclera because of the behavior of stress around any hole (the scleral canal) in a pressurized spherical shell (the posterior scleral shell). Greene used equation 2 to approximate the stresses near the scleral canal and showed that for a circular hole ($a/b = 1$), the stress concentration factor at the edge of the hole is 3.0. Using that equation alone to estimate the maximum level of stress around elliptical scleral canals of small and large aspect ratios suggests that the maximum stress would be approximately 35 × IOP around an elliptical canal with a small aspect ratio (model M8, Fig. 4) and would reach 53 × IOP around an elliptical canal with a large aspect ratio (model M6, Fig. 4).

Although the linear model of a hole in a thin plate provides basic insight into the mechanical conditions surrounding the scleral canal, it is unable to take into account important aspects of the complex 3D anatomy of the ONH—e.g., the curvature of the scleral wall, the variable 3D architecture of the connective tissues within the canal, and the nonhomogeneous material properties of the scleral and laminar extracellular matrix. In our initial attempt to explore these issues, 13 FEMs were used that were based on 13 idealized representations of the human posterior scleral shell.

Within the 13 FEMs of this report, we found that peripapillary scleral stress exhibited maximum levels that varied from 11 × IOP to 20 × IOP when a circular scleral canal was adjusted from 0.50 × 0.50 mm to 2.56 × 2.56 mm, was consistently highest near the superior and inferior poles of vertically elliptical scleral canals, and was additionally increased by elongation of an elliptical canal, increasing the inner radius of the sphere, and decreasing wall thickness. Maximum laminar insertion zone stresses were approximately twice the magnitude of peripapillary scleral stresses in each model and were also influenced by changes in canal geometry, inner radius, and wall thickness. Finally, laminar trabecular stresses were consistently higher than stresses in any other region of the model; were also affected by changes in canal geometry, inner radius, and wall thickness; and demonstrated maximum values as high as 122 × IOP (model M9, Tables 2 and 3).

The magnitude of IOP-related stress within the connective tissues of the ONH has been only indirectly addressed in previous reports. Zeimer[14] discussed the implications of stress within the lamina cribrosa and its relation to the viscoelastic properties of the laminar trabeculae and scleral canal. Dongqi and Zeqin[15] recently published a mathematical model predicting the displacement of a thin circular plate representing an idealized lamina cribrosa. Yablonski and Asamoto[3] have suggested how the interplay between IOP and radius of curvature of the lamina may affect stresses within the load-bearing tissues of the ONH. Yan et al.[16] proposed a laminar model in which stresses (predominantly shearing stresses) are responsible for the observed posterior displacement of the lamina cribrosa at elevated IOP.

Our computational simulations strongly suggest that the level of IOP-related stress for a given level of IOP is principally determined by the 3D geometry of the load-bearing tissues of the ONH. Specifically, ONHs that have large and/or elliptical scleral canals or that are bounded by thin peripapillary and posterior sclera should have higher levels of IOP-related stress for the same level of IOP.

The literature regarding scleral canal size as a risk factor for glaucomatous damage is inconclusive. Several researchers have reported that glaucomatous eyes measured clinically[17–19] and after death[20,21] do not have larger disc diameters, and some have suggested that this implies that scleral canal size is not a risk factor for glaucomatous damage.[10] Chi et al.[22] and others[10] have reported a larger disc area in blacks than in whites. Chi et al.[22] have postulated that this may be one reason why blacks may have a higher susceptibility to glaucomatous damage; however, others have stressed that it is not clear that the ONH in blacks is, in fact, more susceptible to glaucomatous damage.[10] Nesterov and Egorov[23] have suggested that, on a theoretical basis, disc size should be one determinant for susceptibility, and Cahane and Bartov[24] have explored the theoretical implications of both axial length and scleral thickness.

To our knowledge, apart from scleral canal size, scleral canal shape has not previously been considered as a risk factor for glaucomatous damage. Quigley and Addicks[25] and Radius[26] have characterized the difference in laminar beam and axonal fenestration dimensions within the superior–inferior versus the nasal–temporal peripheral scleral canal. Both groups attributed early superior and inferior axonal loss in glaucoma to the relative lack of connective tissue support in these regions. The idealized geometries in our report do not address these differences in 3D laminar anatomy; however, it is hoped that ongoing studies in our laboratories involving geometries derived from 3D reconstructions of serial histologic sections eventually will do so.

Although the current literature has not clearly shown scleral canal size and shape to be risk factors for glaucomatous damage, we believe that conclusions should not be drawn from the group of studies that compare the size of the optic disc in glaucomatous versus nonglaucomatous eyes. Our data do not suggest that glaucomatous eyes should necessarily have larger scleral canals than nonglaucomatous eyes. Rather, our data suggest that among groups of eyes with similar age, severity of disease, and levels of 24-hour IOP exposure, but differing rates of onset and/or progression of glaucomatous damage, those groups with greater rates of damage may demonstrate differences in the size and/or shape of the scleral canal and the thickness of the posterior sclera.

Chisholm et al.[27] reported differences in eye wall stress calculations (but did not study scleral canal size and shape differences) between hypertensive glaucoma suspects in whom disease did or did not progress to glaucomatous damage. However in their study, 24-hour IOP exposure was not longitudinally assessed.

The accuracy of the predictions of an FEM depends on the accuracy of its 3D geometry, the accuracy of its material properties, and the refinement of its element mesh (i.e., the relative size of the individual elements within the model). The FEMs in this report should be considered preliminary and will improve as digital geometries derived from 3D reconstructions of serial histologic sections (Fig. 1F) are implemented and discretized into larger numbers of elements and as the assignment of material properties becomes more realistic.

Within our 13 FEMs, the constituent elements of each model were grouped into posterior scleral, peripapillary scleral, laminar insertion, and laminar trabecular regions (Fig. 5). Although in this report we assigned the same scleral material strength to all connective tissue finite elements of all 13 models, future models will assign separate, nonisotropic material properties to elements within each of these regions, based on their profound extracellular matrix differences.[16,28,29]

Because the geometry of these models does not adequately reflect the complexity of the lamina cribrosa, the location and magnitude of the model's predictions for laminar stress may not be accurate. Within the human scleral canal, the connective tissues that make up the laminar sheets are densely fused into a thick connective tissue coat that surrounds the central retinal vessels. The laminar sheets then progressively attenuate into individual beams that are thinnest at their insertion into the scleral canal wall.[25,26] Because of their thin cross-sectional area, we expect that stresses will be highest within these peripheral laminar beams. However, this basic aspect of the 3D geometry of the lamina cribrosa has not been incorporated into our initial models. In fact, within these models, the smallest beams are found within the central scleral canal, and the stress concentrations found there may thus be artifactual (Fig. 6).

The simple laminar geometry in these models may be responsible for two additional forms of error (Figs. 4 and 6). First, within the elliptical models, the horizontally aligned beams are slightly thinner than those that are vertically aligned, and the resultant differences in laminar beam cross-sectional area may artifactually elevate stresses along the nasal–temporal axis. Second, in all the models, there is slight asymmetry of the beams within the scleral canal that may not be physiologic and may alter the concentration of stress.

Finally, in these linear models, there is a direct relationship between IOP and the magnitude of IOP-related stress. Therefore, the absolute magnitudes of IOP-related stress for IOPs of 30, 45, and 60 mm Hg can be estimated by multiplying the values in Table 2 by 2 (IOP of 30 mm Hg), 3 (IOP of 45 mm Hg), and 4 (IOP of 60 mm Hg), respectively. These linear relationships are approximations and result from the fact that the material properties of these models were deliberately kept linear, elastic, and isotropic. Although we believe that this was a fair first approximation, biologic soft tissues by their nature are viscoelastic and nonisotropic[14] and do not show this linear relationship.

The elastic and viscoelastic material properties of posterior sclera are currently under study.[30] Future inclusion of these viscoelastic material properties along with their nonisotropic assignment will improve the accuracy of the models' predictions and allow the study of risk factors associated with the distribution of connective tissues within the scleral canal that are separate from canal size and shape and scleral wall thickness.

References

1. Maumenee AE. The pathogenesis of visual field loss in glaucoma. In: Brockhurst RJ, Boruchoff SA, Hutchinson BT, Lessell S, eds. *Controversy in Ophthalmology*. Philadelphia: WB Saunders; 1977: 301–311.
2. Maumenee AE. Causes of optic nerve damage in glaucoma: Robert N. Shaffer Lecture. *Ophthalmology.* 1983;90:741–752.
3. Yablonski ME, Asamoto A. Basic sciences in clinical glaucoma: hypothesis concerning the pathophysiology of optic nerve damage in open angle glaucoma. *J Glaucoma.* 1993;2:119–127.
4. Hayreh SS. Pathogenesis of cupping of the optic disc. *Br J Ophthalmol.* 1974;58:863–76.
5. Hayreh SS. Pathogenesis of optic nerve head changes in glaucoma. *Semin Ophthalmol.* 1986;1:1–13.
6. Langham ME. The temporal relation between intraocular pressure and loss of vision in chronic simple glaucoma. *Glaucoma.* 1980; 2:427–435.
7. Cook RD, Malkus DS, Plesha ME. *Concepts and Applications of Finite Element Analysis.* 3rd ed. New York: John Wiley & Sons; 1989.
8. Jonas JB, Gusek GC, Guggenmoos–Holzmann I, Naumann GOH. Size of the optic nerve scleral canal and comparison with intravital determination of optic disc dimensions. *Graefes Arch Clin Exp Ophthalmol.* 1988;226:213–215.
9. Britton RJ, Drance SM, Schulzer M, Douglas GR, Mawson DK. The area of the neuroretinal rim of the optic nerve in normal eyes. *Am J Ophthalmol.* 1987;103:497–504.
10. Quigley HA, Brown AE, Morrison JD, Drance SM. The size and shape of the optic disc in normal human eyes. *Arch Ophthalmol.* 1990;108:51–57.
11. Timoshenko SP, Goodier JN. *Theory of Elasticity.* 3rd ed. New York: McGraw–Hill; 1970.
12. Kobayashi AS, Woo SL-Y, Lawrence C, Schlegel WA. Analysis of the corneo-scleral shell by the method of direct stiffness. *J Biomech.* 1971;4:323–330.
13. Greene PR. Mechanical considerations in myopia: relative effects of accommodation, convergence, intraocular pressure, and the extraocular muscles. *Am J Optom Physiol Opt.* 1980; 57:902–914.
14. Zeimer R. Biomechanical properties of the optic nerve head. In: Drance SM, ed. *Optic Nerve in Glaucoma.* New York: Kugler; 1995:107–121.
15. Dongqi H, Zeqin R. A biomathematical model for pressure-dependent lamina cribrosa behavior. *J Biomech.* 1999;32:579–584.
16. Yan DB, Coloma FM, Metheetrairut A, Trope GE, Heathcote JG, Ethier CR. Deformation of the lamina cribrosa by elevated intraocular pressure. *Br J Ophthalmol.* 1994;78:643–648.
17. Caprioli J, Miller JM. Videographic measurements of optic nerve topography in glaucoma. *Invest Ophthalmol Vis Sci.* 1988;29: 1294–1298.
18. Caprioli J, Miller JM, Sears M. Quantitative evaluation of the optic nerve head in patients with unilateral visual field loss from primary open-angle glaucoma. *Ophthalmology.* 1987;94:1484–1487.
19. Jonas JB, Gusek GC, Naumann GOH. Optic disc morphometry in chronic primary open-angle glaucoma, I: morphometric intrapapillary characteristics. *Graefes Arch Clin Exp Ophthalmol.* 1988; 226:522–530.
20. Quigley HA. Childhood glaucoma: results with trabeculectomy and study of reversible cupping. *Ophthalmology.* 1982;89:219–226.
21. Quigley HA, Hohman RM, Addicks EM, Massof RW, Green WR. Morphologic changes in the lamina cribrosa correlated with neural loss in open-angle glaucoma. *Am J Ophthalmol.* 1983; 95:673–691.
22. Chi T, Ritch R, Stickler D, Pitman B, Tsai C, Hsieh FY. Racial differences in optic nerve head parameters. *Arch Ophthalmol.* 1989;107:836–839.
23. Nesterov AP, Egorov EA. Pathological physiology of primary open angle glaucoma: The optic nerve changes. In: Cairns J, ed. *Glaucoma*. Vol. 1. Orlando, FL: Grune & Stratton; 1986:369–393.
24. Cahane M, Bartov E. Axial length and scleral thickness effect on susceptibility to glaucomatous damage: a theoretical model implementing Laplace's law. *Ophthalmic Res.* 1992;24:280–284.
25. Quigley HA, Addicks EM. Regional differences in the structure of the lamina cribrosa and their relation to glaucomatous optic nerve damage. *Arch Ophthalmol.* 1981;99:137–143.
26. Radius RL. Regional specificity in anatomy at the lamina cribrosa. *Arch Ophthalmol.* 1981;99:478–480.
27. Chisholm IA, Drance SM, Chauhan BC. The glaucoma suspect: differentiation of the future glaucomatous eye from the non-glaucomatous suspect eye. *Graefes Arch Clin Exp Ophthalmol.* 1989; 227:17–20.
28. Morrison JC. The microanatomy of the optic nerve. In: Drance SM, Anderson DR, eds. *Optic Nerve in Glaucoma*. New York: Kugler; 1995:57–78.
29. Hernandez MR, Gong H. Extracellular matrix of the trabecular meshwork and optic nerve head. In: Ritch R, Shields MB, Krupin T, eds. *The Glaucomas: Basic Sciences*. Vol. 1, 2nd ed. St. Louis, MO: Mosby-Year Book; 1996:213–249.
30. Downs JC, Burgoyne CF, Thomas KA, et al. Effects of strain rate on the mechanical properties of posterior rabbit sclera (abstract). *Biomedical Engineering Society*, Atlanta, GA, October, 1999.